Kovove Mater. 60 2022 67–78
DOI: 10.31577/km.2022.2.67

Creep behavior and microstructural characterization of iron-nickel and nickel-based superalloys

Vagner João Gobbi[1], Silvio José Gobbi[1], Danieli Aparecida Pereira Reis[2], Jorge Luiz de Almeida Ferreira[1], José Alexander Araújo[1], Cosme Roberto Moreira da Silva[1]*

[1] *Faculty of Technology, University of Brasilia – UnB, Brasilia 70910-900, Brazil*
[2] *Science and Technology Department, Universidade Federal de São Paulo – UNIFESP, São José dos Campos 12231-280, Brazil*

Received 26 January 2022, received in revised form 3 May 2022, accepted 3 May 2022

Abstract

New superalloys are constantly being developed to fulfill the increased demand for alloys with high creep resistance and low manufacturing costs. This study subjected two alloys to comparative creep tests and microstructural characterization. A novel low-cost iron-nickel superalloy with intermediate Ni and Fe content was designated in this work as Fe-Ni-Cr and the NIMONIC 80A with a high Ni. Creep experiments were carried out at temperatures ranging from 650 to 750 °C and loads ranging from 500 to 600 MPa. Microstructural characterization and surface analysis were carried out using microscopy techniques such as optical, SEM with EDS, and TEM. For phase quantitative identification, Rietveld refinement was utilized. Compared to NIMONIC 80A, the new Fe-Ni-Cr superalloy showed higher creep resistance. The Fe-Ni-Cr alloy has higher percentages of carbon and iron and the addition of niobium, resulting in the formation of γ' intermetallics and carbides rich in iron and niobium. These carbides and intermetallics operate as obstacles to dislocation glide and climb, lowering the creep rate. Compared to Fe-Ni-Cr, the reduced carbides in NIMONIC 80A promote relative slip between grains during deformation, facilitating creep rate acceleration and early failure.

K e y w o r d s: creep, superalloy, iron-nickel

1. Introduction

There has been a remarkable advancement in the development of superalloys for high-temperature applications [1–5]. A new superalloy has enhanced power in aviation turbines while lowering fuel consumption [6–9]. Nickel-based alloys have been employed in high-temperature engine components due to their outstanding resistance to fatigue and creep and minimal thermal expansion [8–10]. The production of the γ' phase (Ni_3Al, Ni_3Ti, $Ni_3(Al,Ti)$) and carbides with high thermal stability causes creep resistance in these alloys [10, 11]. However, adding an appreciable amount of nickel and other alloying elements is necessary to achieve this performance, with a consequent increase in their production costs [11]. There is, therefore, growing interest in superalloys with good creep resistance and lower costs. This case includes iron-nickel superalloys used in systems that require low thermal expansion, such as high-performance automotive valves, turbine blades, discs, and engine casings [11, 23]. The Al, Nb, Ti, Mo, and Cr alloy elements are used to manufacture these superalloys aiming to form phases that increase the mechanical properties at high temperatures [12]. The partial replacement of iron with nickel and the inclusion of various alloying elements results in solid solution reinforcement and improves creep resistance in these alloys. It also prevents the creation of harmful TCP phases [13–15]. In addition to carbides and carbonitrides dispersed in the grain and grain boundaries [16–18], some Fe-Ni superalloys include intermetallic precipitates of spheroid form γ'-$Ni_3(Al,Ti)$, with fcc structure and coherent with the γ solid solution. Dislocation slip prevails for some stress and temperature conditions [18–19]. This slip can be affected by the formation of intergranular

*Corresponding author: tel.: +55-61-31071144; e-mail address: cosmeroberto@gmail.com

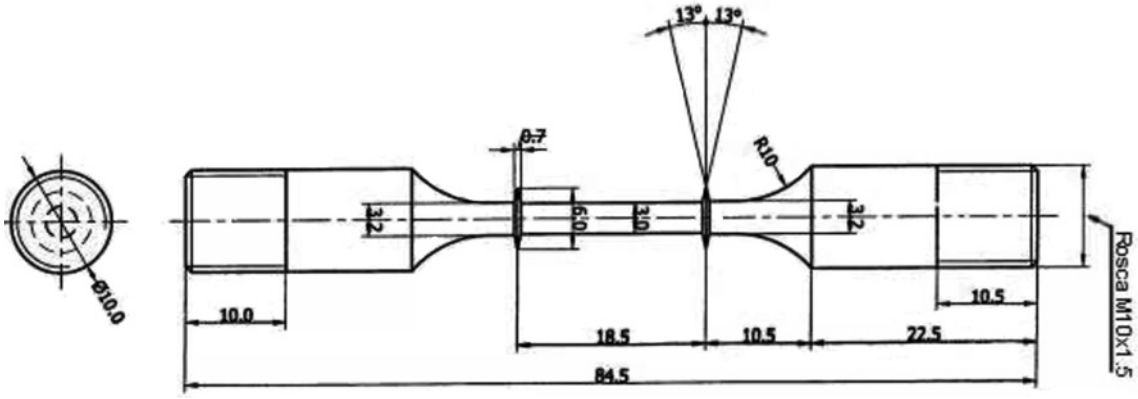

Fig. 1. Geometry and dimensions of the specimen used in the creep tests.

or transgranular carbides, present in both Ni-based and Fe-Ni superalloys. When continuing, the slide is difficult due to the presence of carbides, the dislocation will climb, which, because it is a slower process, will operate as the rate-controlling deformation mechanism [18–23]. Given the impact of carbides and intermetallics on mechanical properties at high temperatures, it's reasonable to assume that the volume fraction, coherence, and position of these carbides and intermetallics will influence the creep rate of superalloys. The goal of this study was to carry out a comparative creep test and microstructural characterization of new lower-cost nickel superalloy Fe-Ni-Cr with intermediate Ni and Fe content, with the standard nickel-based superalloy NIMONIC 80A, which has a high nickel content and a higher production cost. Both alloys feature an austenitic matrix with intermetallic compounds and carbides dispersed throughout. Creep experiments were carried out at temperatures ranging from 650 to 750 ℃ and loads ranging from 500 to 600 MPa.

2. Experimental procedures

The superalloys Fe-Ni-Cr and NIMONIC 80A produced in cylindrical bars were used to carry out this work. Specimens were prepared from the bars to conduct creep tests according to the ASTM E21-20 Standard (Standard Test Methods for Elevated Temperature Tension Tests of Metallic Materials). After production, the specimens were subjected to solubilization and vacuum aging heat treatments. The creep tests were carried out in MAYES furnaces at temperatures ranging from 675 to 750 ℃ and stresses in the 500–600 MPa range. The dimensions and geometry of creep specimens are specified in Fig. 1.

For creep tests, a G28 3181-16 cylindrical furnace was used. Through an electrical system and a controller, the working temperatures presented a variation of ± 2 ℃, according to the ASTM E139/83 standard. For data acquisition related to the specimen's elongation and for the temperature measurements in predetermined periods, the Antares Software was used. Elongation measurements were obtained using an LVDT Schlumberger D6.50 transducer with an output voltage of 53.18 mV V^{-1} mm^{-1}. For temperature control, a Chromel-Alumel AWG24 thermocouple was used. Coupled with the controller and a digital temperature indicator installed next to the testing machine, a thermocouple was positioned near the specimen. Antares Software collected the thermocouple signal through a processing unit, with temperature and elongation data stored simultaneously during the creep test. The extensometer to obtain the elongation measurements consisted of a set of rods, which moved parallel to the specimen as the sample elongated during the test. These rods were fixed to an LVDT type transducer attached to the bottom of the extensometer, outside the heating zone, in an environment maintained at around 35 ℃. The LVDT output signal was sent to a processing unit, which converted the signals into elongation measurements for periods pre-defined by the operator and fed the Antares Software. The X-ray diffraction was carried out with a Philips model PW 3710 diffractometer. An angular range of $10° \leq 2\theta \leq 125°$ and CuK radiation (λ = 1.54184 Å) were applied as operational conditions. The Optical and Scanning Electron Microscopy (SEM) analysis samples were prepared according to standard metallography procedures, including mounting in resin and manual grinding with SiC-based sandpaper in a sequence ranging from 120 to 2400. After that, polishing with 6, 3, and 1 μm diamond paste was done, followed by Kalling reagent chemical etching. The scanning microscopes Quanta 200 3D from PHILIPS, JEOL/JSM-700 IF, and JEOL/JSM 6490-LV were utilized for SEM and Energy Dispersive X-Ray Spectroscopy (EDS) analyses. The transmission electron microscopy images (TEM) were taken using a JEOL/JEM – 2100 microscope. Initially, a cut was made with a precision diamond disc to produce

Table 1. Chemical composition: Fe-Ni-Cr and NIMONIC 80A (mass%)

Alloys	Elements	
	Fe-Ni-Cr	NIMONIC 80A
Ni	32.00	75.70
Fe	44.14	2.00
Cr	15.80	18.60
C	0.26	0.05
Ti	2.00	2.25
Nb	3.90	–
Al	1.90	1.40

1 mm thick plates to prepare the samples for TEM investigation. Electrical Discharge Machine (EDM) was used to make 3 mm diameter discs from these plates. The discs were then ground to 100 micrometers with 600 particle-size sandpaper. Electrolytic polishing was performed in the final phase, employing a 20 percent ethyl alcohol (C_2H_5OH) solution with 80 percent perchloric acid ($HClO_4$) and a voltage of up to 25 mV.

3. Results and discussion

3.1. Chemical composition

Table 1 shows the chemical compositions of the alloys Fe-Ni-Cr and NIMONIC 80A. Table 1 shows the nickel, iron, carbon, and niobium content differences between the two compositions. In addition to the presence of niobium, Fe-Ni-Cr has a lower Ni content and a substantially higher percentage of carbon and iron. Because of their solid chemical affinities, Ti and Nb preferentially mix with carbon to create carbides when added to the alloy. The remaining percentage of these two elements in the Fe-Ni-Cr alloy that did not participate in carbide formation develop intermetallic phases with nickel (NiTi and NiNb). Aluminum improves alloy mechanical strength at high temperatures by reacting with nickel to form an intermetallic phase and enhancing oxidation resistance by creating Al_2O_3 during heating. Chromium increases corrosion and oxidation resistance at high temperatures by creating Cr_2O_3.

3.2. Microstructural analysis of the NIMONIC 80 A superalloy

Figure 2 shows the scanning microstructure of the NIMONIC 80A alloy. Carbides are mainly dispersed at grain boundaries. Therefore, one precipitate (arrow) was selected for EDS analysis.

The EDS spectrum performed in the area where the precipitate in Fig. 2 reveals Ni present in the matrix and high chromium and carbon contents (Fig. 3), consistent with the formation of chromium-rich carbides in the grain boundaries of the NIMONIC 80 A alloy.

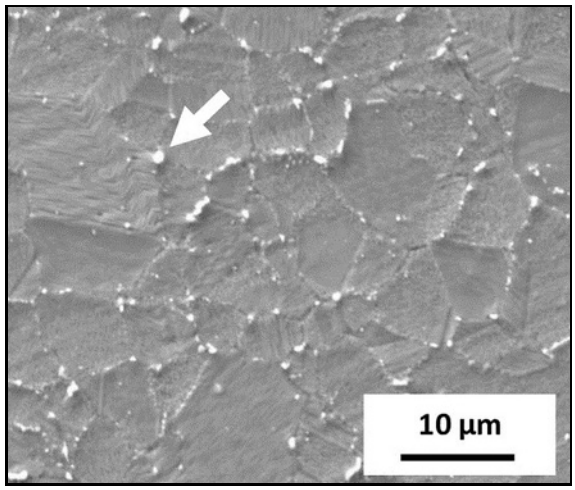

Fig. 2. Electron scanning micrograph of the NIMONIC 80 A sample, showing M23C6 type carbides distributed evenly along the grain boundaries and the precipitate at the grain boundary selected for EDS analysis (an arrow).

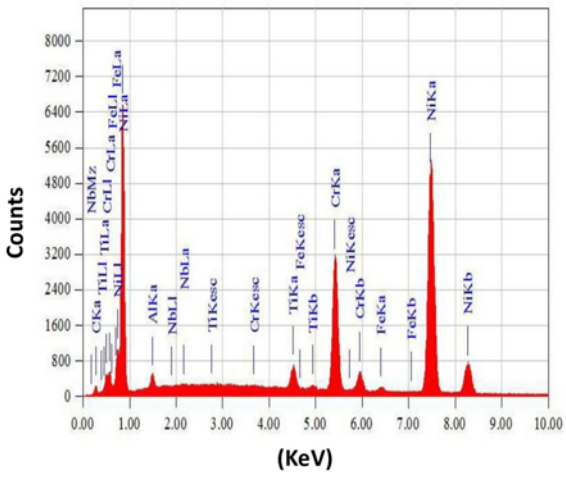

Fig. 3. EDS spectrum corresponding to the NIMONIC 80 A region containing the precipitate indicated by the arrow in Fig. 2 consistent with the composition of chromium-rich carbides at grain boundaries and nickel-chromium matrix.

Table 2 presents the quantitative EDS analysis of the spectrum observed in Fig. 3, corresponding to the matrix based on nickel and chromium carbides.

Figure 4, as seen by TEM, depicts intermetallic compounds γ' and carbides in the grain boundaries of the NIMONIC 80 A alloy.

3.3. Microstructural analysis of the Fe-Ni-Cr superalloy

The microstructures and microstructural analy-

T a b l e 2. Quantitative EDS analysis for grain boundaries carbides of Nimonic 80A

Element	(keV)	(mass%)	Sigma	(at.%)
C	0.277	5.38	0.11	21.03
Al	1.486	1.02	0.04	1.78
Ti	4.508	2.28	0.05	2.24
Cr	5.411	18.36	0.15	16.58
Fe	6.398	0.77	0.04	0.65
Ni	7.741	72.12	0.40	57.69
Nb	2.166	0.07	0.04	0.03
Total	–	100.00	–	100.00

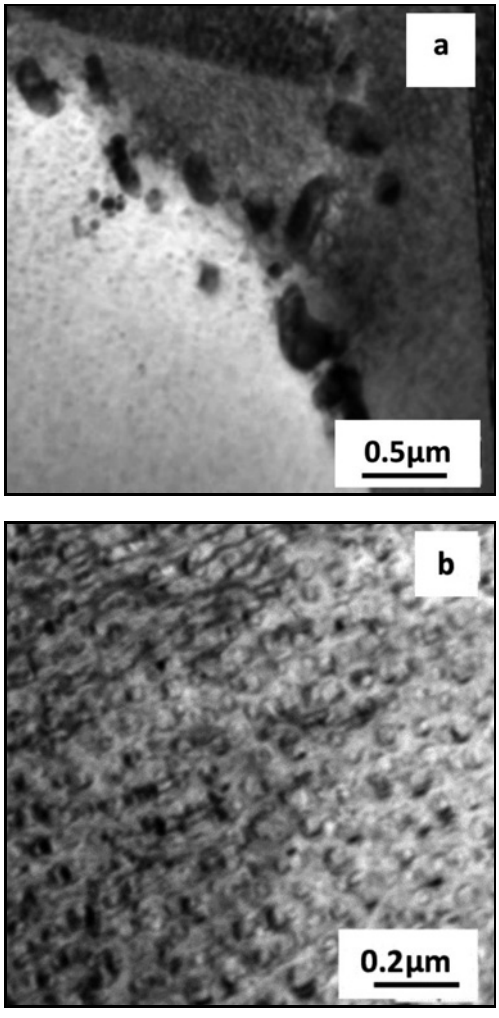

Fig. 4. TEM micrograph (bright-field images) of the NIMONIC 80A superalloy showing carbides at grain boundaries (a) and uniform distribution of fine gamma prime precipitates (γ' intermetallic compounds) (b).

sis of the Fe-Ni-Cr alloy are depicted in the following figures. Optical and scanning microscopy analyses

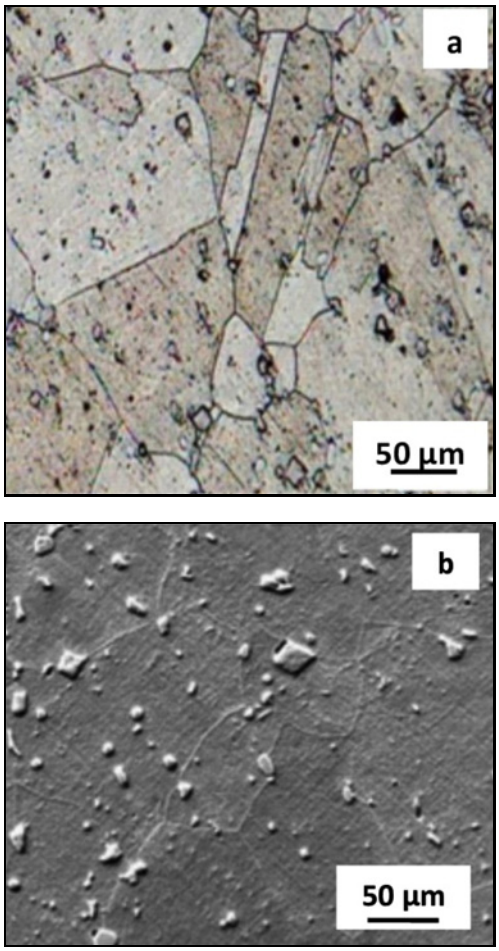

Fig. 5. Optical (a) and scanning electron micrograph (b) of Fe-Ni-Cr superalloy with intergranular and intragranular precipitates.

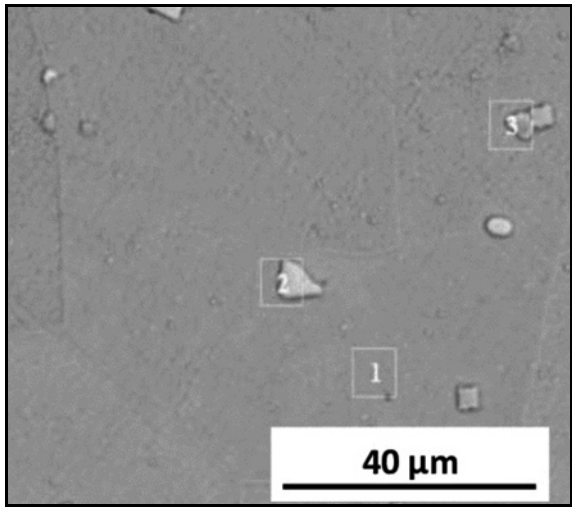

Fig. 6. Scanning electron micrograph of Fe-Ni-Cr sample with regions analyzed by EDS: matrix (1) and precipitates (2) and (3).

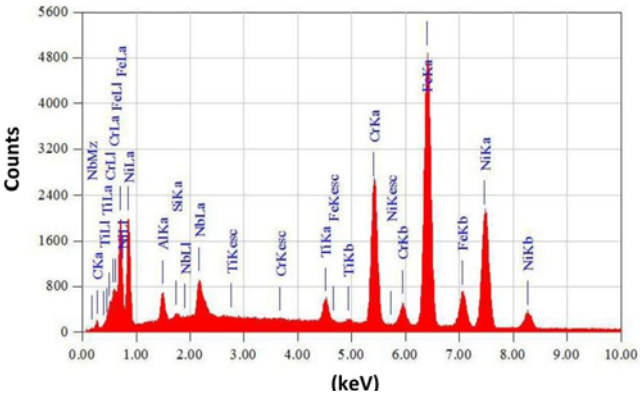

Fig. 7. EDS spectrum corresponding to region 1 (matrix) of Fig. 6.

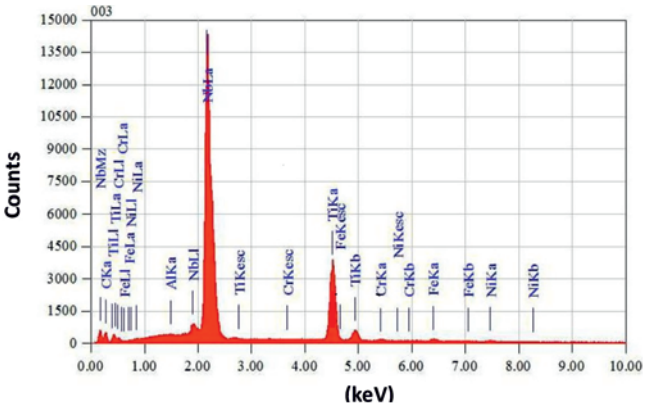

Fig. 8. EDS spectrum for the precipitate from region 2 of Fig. 6.

Table 3. EDS quantitative analysis of Fe-Ni-Cr alloy

Element	(keV)	(mass%)	Sigma	(at.%)
C	0.277	3.33	0.08	13.77
Al	1.486	1.58	0.05	2.92
Si	1.739	0.24	0.03	0.42
Ti	4.508	1.89	0.05	1.96
Cr	5.411	15.18	0.13	14.53
Fe	6.398	43.53	0.26	37.88
Ni	7.741	30.88	0.27	26.17
Nb	2.166	4.37	0.09	2.34
Total	–	100.00	–	100.00

Table 4. Quantitative EDS analysis of the precipitate observed in the Fe-Ni-Cr alloy

Element	(keV)	(mass%)	Sigma	(at.%)
C	0.277	15.70	0.23	54.0
Al	1.486	0.05	0.02	0.08
Ti	4.508	18.43	0.14	15.92
Cr	5.411	0.34	0.03	0.27
Fe	6.398	0.93	0.04	0.69
Ni	7.741	0.75	0.05	0.53
Nb	2.166	63.80	0.25	28.42
Total	–	100.00	–	100.00

(Fig. 5) revealed a large number of precipitates dispersed both in the matrix and at the grain boundaries.

A section of the matrix (region 1) and two precipitates (regions 2 and 3) of the Fe-Ni-Cr superalloy sample were chosen to identify the elements present in each case, as shown in Fig. 6.

The EDS analysis of the matrix selected in Fig. 6 revealed a high iron and nickel content consistent with the primary constituents of an austenitic iron-nickel-chromium alloy (Fig. 7).

Table 3 presents the quantitative EDS analysis of the spectrum corresponding to the matrix based on nickel and chromium carbides of Fe-Ni-Cr alloy.

The spectrum in Fig. 8 shows the presence of carbon and an increased amount of Nb and Ti in the precipitate found in region 2 of Fig. 6, which is consistent with the composition of (Nb,Ti)C.

Table 4 presents the EDS quantitative analysis of precipitate 2, revealing high carbon, niobium, and titanium levels compatible with (Nb,Ti)C.

The EDS spectrum of the precipitate from area 3 in Fig. 6 was similar to that of the precipitate from region 2, with substantial amounts of Nb and Ti, indicative of (Nb,Ti)C carbides. Figure 9 displays transmission electron microscopy images of Fe-Ni-Cr, which exhibit carbides and intermetallic complexes gamma prime (γ'): (a) bright-field image and (b) dark-field image.

3.4. Rietveld refinement

The peaks corresponding to the γ' intermetallic compounds $Ni_3(Al,Ti)$, $Ni_3(Al_{0.5}Ti_{0.5})$ are overlaid on the austenitic matrix's (γ) most significant peak. The Rietveld method was used (Figs. 10 and 11) to refine the crystal structure because it was difficult to discriminate between the γ and intermetallic phases due to the proximity of its lattice parameters [24–26]. The lattice parameters and phase percentages for the alloys NIMONIC 80A and Fe-Ni-Cr are listed in Table 5.

In the microscope images shown in Fig. 2, the alloy NIMONIC 80A has the highest proportion of the gamma prime phase and a limited quantity of chromium carbide, which is primarily dispersed in the grain boundary. On the other hand, Ni and Ti carbides and two forms of gamma prime phase predomi-

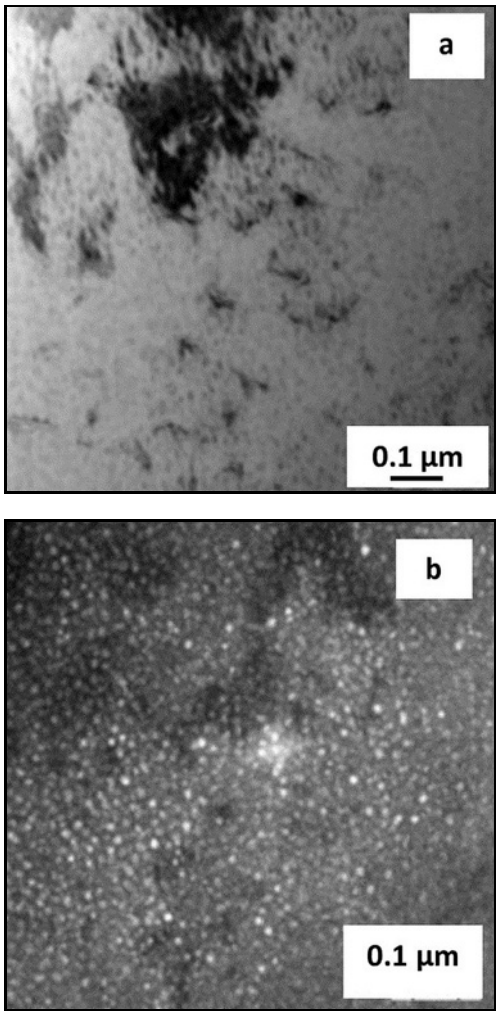

Fig. 9. TEM micrograph of Fe-Ni-Cr superalloy showing carbides (a) and gamma prime (γ') intermetallic compounds (b) in bright-field and dark-field, respectively.

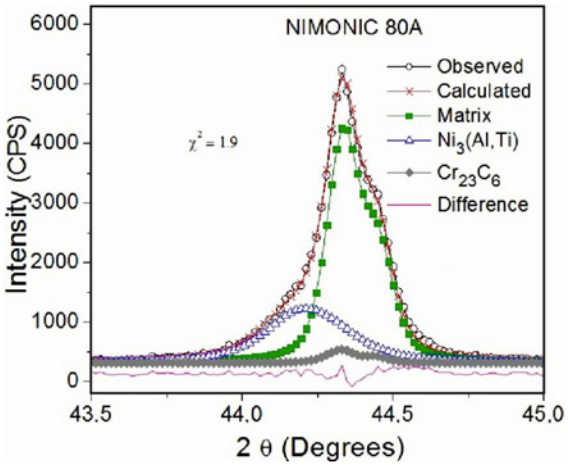

Fig. 10. Rietveld refinement carried out near the angular range $43.5° \leq 2\theta \leq 45.0°$ for NIMONIC 80A alloy.

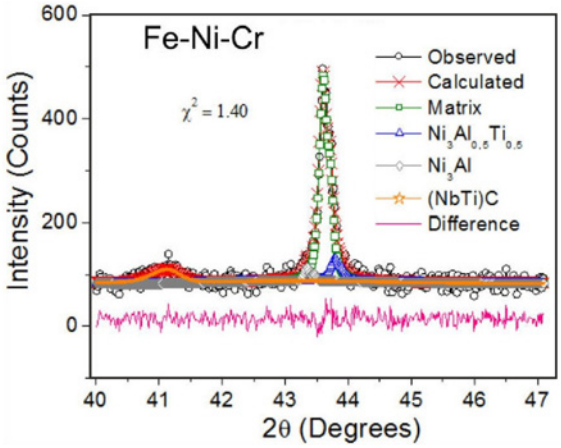

Fig. 11. Rietveld refinement was performed at $40° \leq 2\theta \leq 47°$ for the Fe-Ni-Cr alloy.

Table 5. Lattice parameters and phase percentages for NIMONIC 80A and Fe-Ni-Cr alloys

NIMONIC 80A		
Phases	(wt.%) calculated	Lattice parameters (Å)
Matrix (γ)	65	$a = b = c = 3.535$
$Ni_3(AlTi)(\gamma')$	32	$a = b = c = 3.551$
$Cr_{23}C_6$	3	$a = b = c = 10.605$
Fe-Ni-Cr		
Phases	(wt.%) calculated	Lattice parameters (Å)
Matrix (γ)	65	$a = b = c = 3.590$
$Ni_3(Al_{0,5}Ti_{0,5})(\gamma')$	14	$a = b = c = 3.611$
$Ni_3Al(\gamma')$	12	$a = b = c = 3.581$
(NbTi)C	9	$a = b = c = 4.384$

nate in the alloy Fe-Ni-Cr. In this alloy, intermetallics and carbides are evenly distributed within the grains and grain boundaries, affecting its creep resistance.

3.5. Creep tests

Figures 12–14 depict the deformation (ε) vs. time (t) curves for the alloys NIMONIC 80A and Fe-Ni-Cr, subjected to creep tests at temperatures ranging from 675–750 ℃ and stresses ranging from 500 to 600 MPa.

Table 6 presents the creep data at the temperatures and stresses tested.

Fe-Ni-Cr has significantly lower creep rates than NIMONIC 80 A. It is due to a higher content of carbides (Nb,Ti)C in the matrix and grain boundaries for this alloy, as evidenced by microscopic images and

Table 6. Data from creep tests of alloys NIMONIC 80A and Fe-Ni-Cr at temperatures (T) of 675, 700, and 750 °C and stresses (σ) of 500, 550, and 600 MPa, showing creep rate ($\dot{\varepsilon}_s$) and time for failure (t_f) at the fracture site

T (°C)	Material	σ (MPa)	$\dot{\varepsilon}_s$	t_f (h)
675	NIMONIC 80A	500	6.02×10^{-3}	15.94
		550	1.24×10^{-2}	6.79
		600	3.19×10^{-2}	4.04
	Fe-Ni-Cr	500	5.08×10^{-5}	214.58
		550	1.75×10^{-4}	102.33
		600	7.56×10^{-4}	3.96
700	NIMONIC 80A	500	8.89×10^{-2}	1.27
		600	1.14×10^{-1}	0.843
		650	3.16×10^{-1}	0.571
	Fe-Ni-Cr	500	4.40×10^{-4}	25.16
		550	1.55×10^{-3}	14.57
		600	5.93×10^{-3}	1.43
750	NIMONIC 80A	500	5.36×10^{-1}	0.342
		550	10.36×10^{-1}	0.142
		600	20.36×10^{-1}	0.072
	Fe-Ni-Cr	500	2.15×10^{-2}	1.73
		550	8.43×10^{-2}	0.53
		600	2.37×10^{-1}	0.26

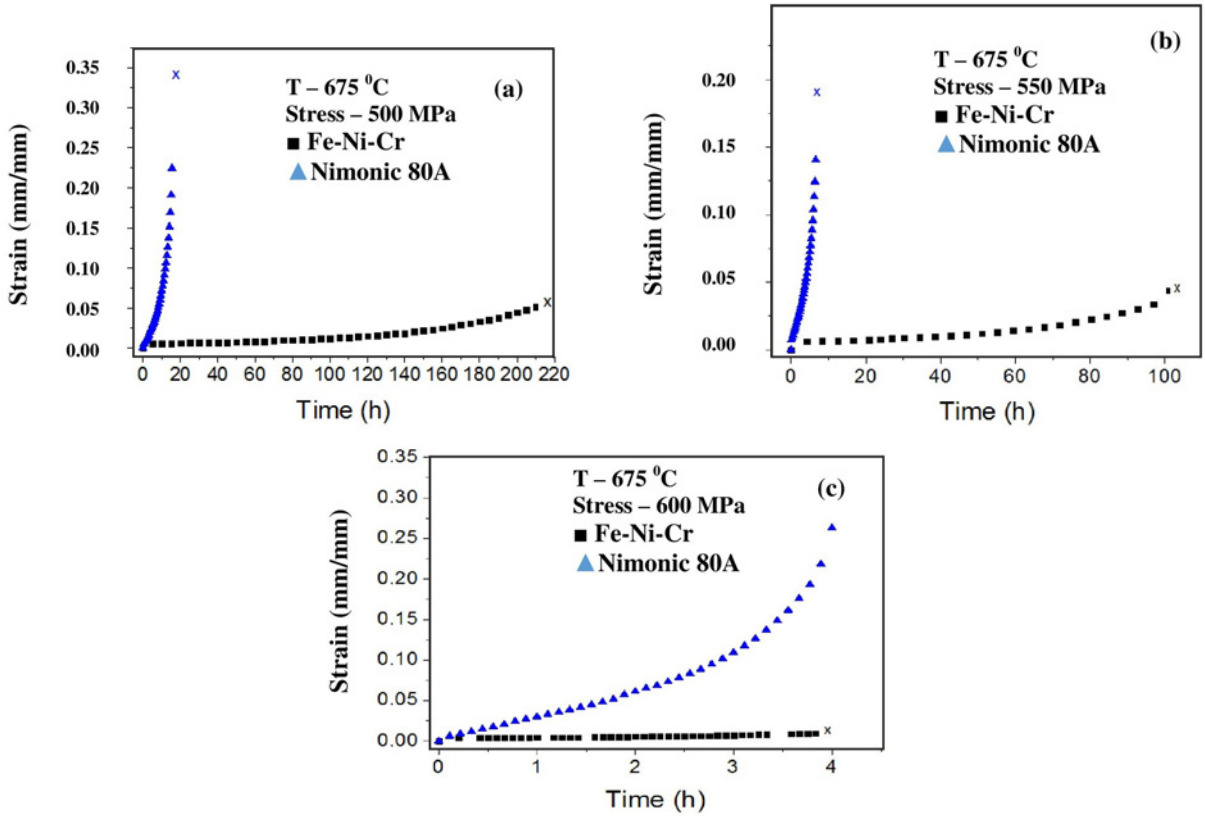

Fig. 12. Creep curves of NIMONIC 80A and Fe-Ni-Cr alloys at 675 °C for stresses of (a) 500, (b) 550, and (c) 600 MPa.

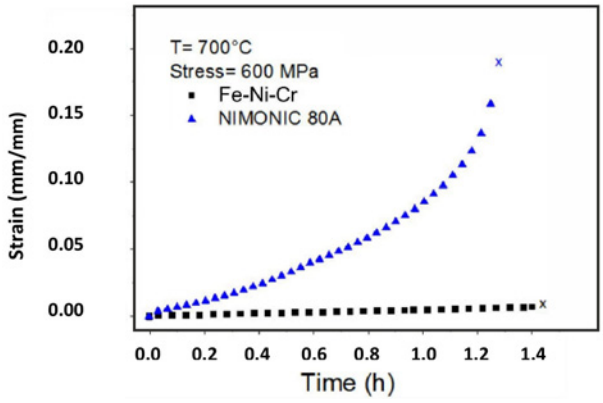

Fig. 13. Creep curves of the NIMONIC 80A and Fe-Ni-Cr alloys at 700 °C and 600 MPa stress.

quantitative analysis using Rietveld refinement.

These precipitates are stable and have a low coalescence rate. As a result, during creep deformation, the movement of dislocations in the sliding planes is hampered by carbides and intermetallics that act as barriers to their passage [27]. Carbides also have an anchoring effect, hindering the relative grain boundary sliding and reducing diffusional processes and dislocation gliding and climbing associated with creep deformation. Fe-Ni-Cr also had the largest mismatch between the lattice parameters γ/γ' (0.58 percent). For the NIMONIC 80A, this mismatch is 0.45 percent. Equation (1) determines this mismatch between lattice parameters, called misfit (δ):

$$\delta = \frac{(a_{\gamma'} - a_{\gamma})}{(a_{\gamma'} + a_{\gamma})}, \tag{1}$$

where $a_{\gamma'}$ and a_{γ} are respectively the lattice parameters of the gamma prime (γ') and gamma (γ) phases. Alloys with a greater difference between lattice parameters have better creep resistance due to the hardening effect provided by modulus misfit strengthening [24–26]. The stationary creep rate's dependence on stress and temperature can be stated as an Arrhenius-type relationship, as shown in Eq. (2) [24]:

$$\dot{\varepsilon}_{\mathrm{s}} = B_0 \sigma^n \exp\left(\frac{-Q_{\mathrm{c}}}{RT}\right), \tag{2}$$

where B_0 is a factor dependent on the stress and structure of the material, σ the applied stress, R the gas constant, and T the absolute temperature. Thus, the concept of a creep mechanism can be characterized by different stress exponent n combined with the activation energy Q_{c}, indicating the dependence of different stress and temperature regimes. Q_{c} and n were calculated using the data in Table 6 and Figs. 15 and 16.

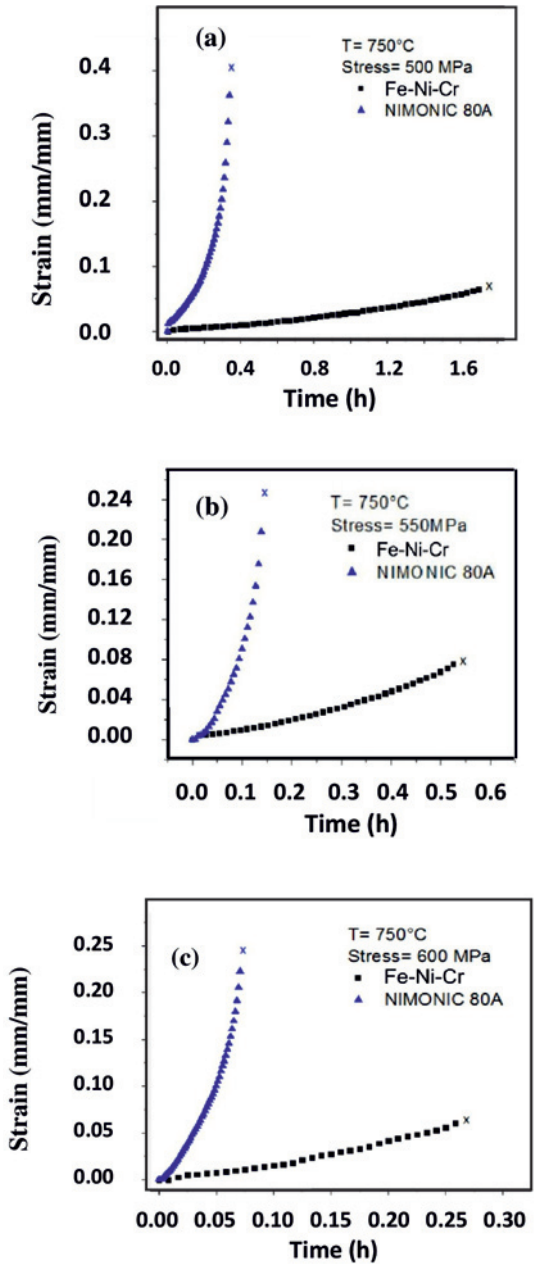

Fig. 14. Creep curves of NIMONIC 80A and Fe-Ni-Cr alloys at 750 °C for stresses of (a) 500, (b) 550, and (c) 600 MPa.

NIMONIC 80A had a stress exponent of 9.12, and Fe-Ni-Cr had a value of 14.80 at 675 °C. It was 14.18 for the Fe-Ni-Cr at 700 °C. The Fe-Ni-Cr had a stress exponent of 13.18 at 750 °C, while the NIMONIC 80A had a stress exponent of 7.30. The activation energy for Fe-Ni-Cr was 616.24 kJ mol^{-1} at 600 MPa and 453.73 kJ mol^{-1} for NIMONIC 80A. For 550 MPa, this energy was 645.34 kJ mol^{-1} for Fe-Ni-Cr and 476.03 kJ mol^{-1} for NIMONIC 80A. Fe-Ni-Cr reached 649.30 kJ mol^{-1} at 500 MPa, while NIMONIC 80A attained 481.95 kJ mol^{-1}. Dislocation creep is a

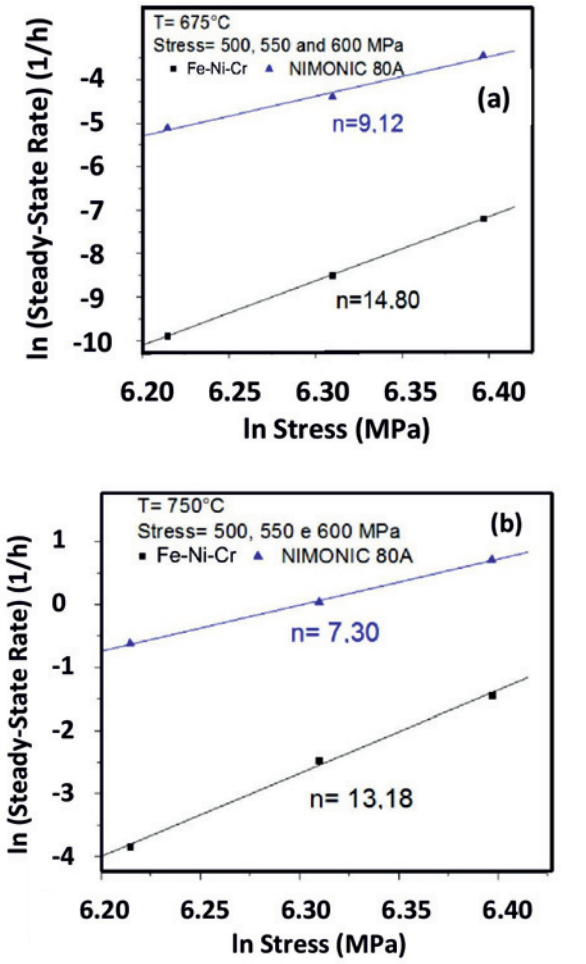

Fig. 15. Dependence of the stationary creep rate on the applied stress for the alloys Fe-Ni-Cr and NIMONIC 80A: (a) 675 °C and (b) 750 °C.

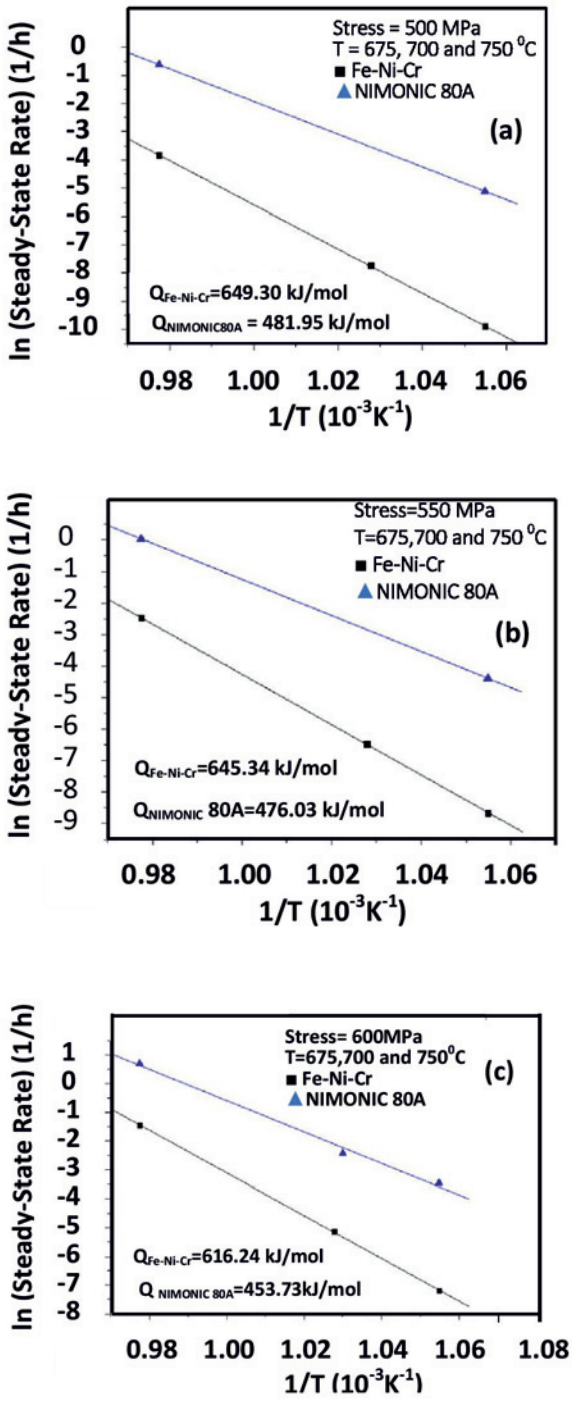

Fig. 16. Temperature dependence of stationary creep rate for and NIMONIC 80A alloys: (a) 500 MPa, (b) 550 MPa, and (c) 600 MPa.

mechanism involving the motion of dislocations. Dislocations can move by gliding in a slip plane, requiring lower thermal activation, as observed for NIMONIC 80A. However, obstacles in the slip plane, such as other dislocations or carbides, can change the rate-determining mechanism of the climbing process, as observed for Fe-Ni-Cr. In this case, the higher exponent for Fe-Ni-Cr can mean the occurrence of an obstacle-controlled dislocation glide mechanism.

Figure 17 shows micrographs of the Fe-Ni-Cr superalloy tested at 500 MPa taken with a transmission electron microscope (bright-field image), revealing dislocations trapped in intermetallic phases (Fig. 17a) and dislocations pile up along the grain boundary (Fig. 17b). These carbides ((Nb,Ti)C), in addition to the γ' intermetallics ($Ni_3(Al_{0.5}Ti_{0.5})$ and Ni_3Al), present both within the grain and its boundary, hinder the movement of dislocations, resulting in a decreased creep rate observed for that superalloy.

3.7. Analysis of fracture surfaces

Figures 18–20 depict the fracture surfaces of the materials investigated. Fe-Ni-Cr exhibits intergranular fracture (Figs. 18, 19), particularly in the region of failure initiation, with progression to a transgranular mode in the final region.

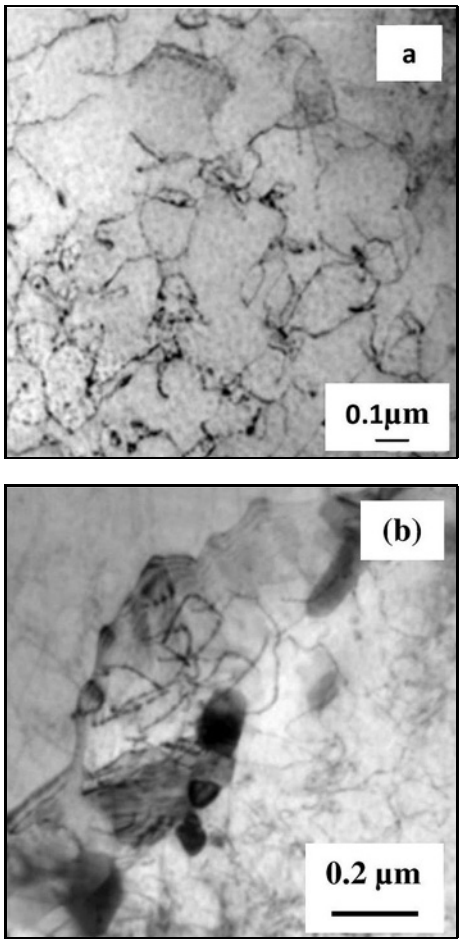

Fig. 17. TEM micrographs (bright-field image) of Fe-Ni-Cr superalloy tested at 500 MPa at temperatures of (a) 750 °C and (b) 675 °C.

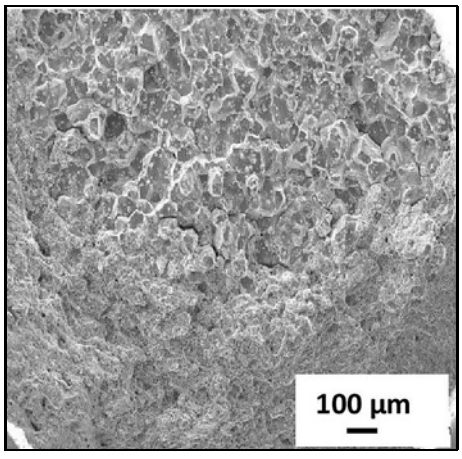

Fig. 18. Intergranular fracture and ductile transgranular aspects of the Fe-Ni-Cr sample's fracture surface tested at 675 °C and 550 MPa.

Figure 19 shows the fracture surface of the Fe-Ni-Cr alloy, tested at 700 °C and 550 MPa, in greater detail, in the region of the onset of the failure with an intergranular aspect (a) and dimples typical of ductile fracture in the final part of the failure (b).

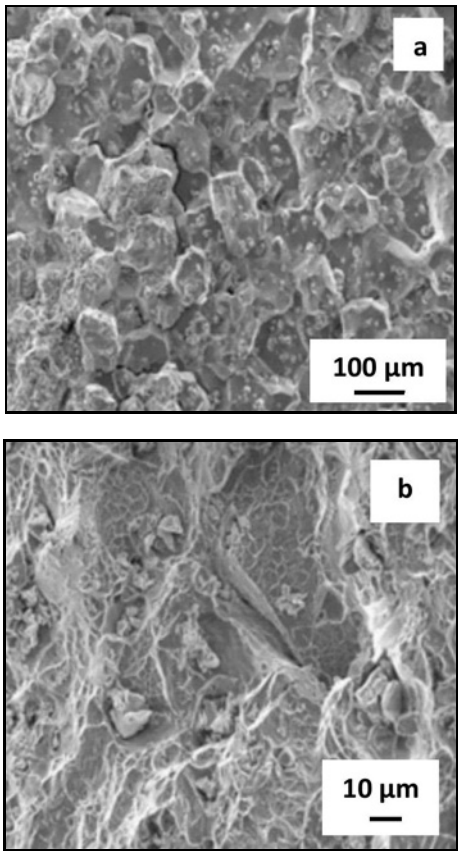

Fig. 19. Fracture surface of the Fe-Ni-Cr sample tested at 700 °C, with an intergranular aspect in the vicinity of the onset of failure (a) and a predominance of dimples, indicative of ductile fracture in the final region of failure (b). In addition, carbides can be found in the alveoli.

As seen in Fig. 20, the fracture surfaces of the NIMONIC 80A alloy were mostly transgranular.

The increased ductility and lower carbides in NIMONIC 80A contribute to the prevalence of ductile transgranular fracture. The microcavities occur at the matrix-intermetallics-carbides interfaces, where there is a stacking of dislocations and localized stresses, resulting in the nucleation and formation of dimples to relieve the stresses. These dimples' size, form, and distribution are related to the material's ductility and internal stresses.

4. Conclusions

1. The microstructure of the alloy NIMONIC 80A shows a small number of carbides, which are preferentially distributed in grain boundaries. As for the Fe-Ni-Cr alloy, both intermetallics and carbides are in greater quantity and evenly distributed within the

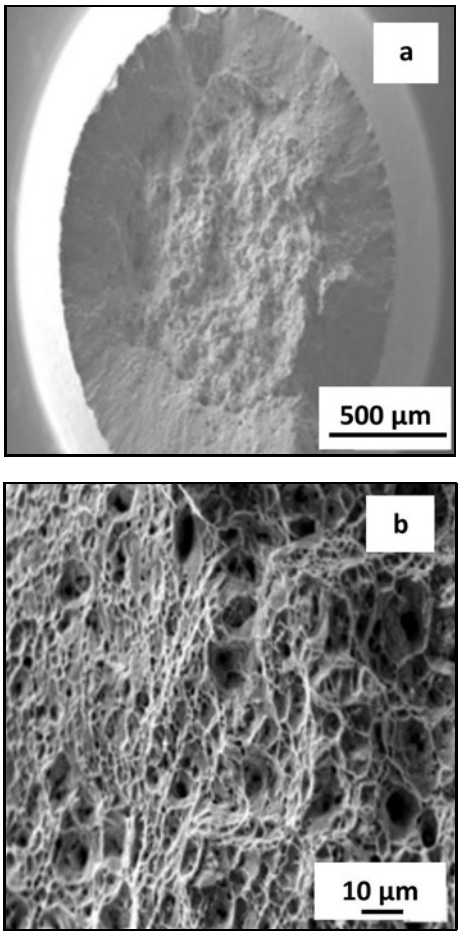

Fig. 20. The surface of the NIMONIC 80A sample (a) tested under creep at 675 °C and 550 MPa shows a transgranular aspect. A detailed image of the fracture surface of this sample (b) has dimples, which are typical for ductile fracture.

grain and at the grain boundaries of the austenitic matrix.

2. Rietveld refinement was used to quantify the carbides and intermetallic precipitates identified in the two alloys. The intermetallic $Ni_3Al(\gamma')$ and $Cr_{23}C_6$ carbides were observed in NIMONIC 80 A. In addition, the intermetallics $Ni_3(Al_{0.5}Ti_{0.5})(\gamma')$ and $Ni_3Al(\gamma')$ were revealed in Fe-Ni-Cr, as well as a significant number of carbides (NbTi)C.

3. With a value nearing 0.58 percent, Fe-Ni-Cr exhibited the most significant misfit (δ) of the lattice parameters γ/γ'. This value is 0.45 percent for the NIMONIC 80A. Due to the hardening effect given by modulus misfit strengthening, alloys with a more significant mismatch between lattice parameters have higher creep resistance.

4. The lower carbide content in NIMONIC 80 A and its distribution primarily at grain boundaries increase relative slip between grains during deformation, allowing grain boundary sliding for the formation of intergranular cracks and, as a result, increasing creep rate and premature rupture.

5. As for Fe-Ni-Cr, a high volume fraction of intermetallics and carbides was observed, affecting the mobility of dislocations. The low diffusion rates and high stability of these phases hinder the glide of dislocations within the grain and along the grain boundary during creep tests by switching the creep mechanism from the dislocation glide to the slower dislocation climb. The dislocation climb requires a void to be displaced to its core, allowing it to slide to an adjacent sliding plane.

6. Grain boundary sliding requires a constant supply of dislocations from the matrix. The presence of intermetallics and carbides within the grain might impact the glide of these dislocations, resulting in pile-ups with back stress, as observed in Fe-Ni-Cr alloy. As a result, the effective stress at the grain interface is lowered during the creep test, slowing the sliding rate of the grain boundaries.

7. The stress exponents ranged from 7.3 to 14.8, with activation energies ranging from 453–649 kJ mol^{-1}. These values are higher than the activation energy for nickel lattice diffusion (280 kJ mol^{-1}) and significantly higher than grain boundary self-diffusion (115 kJ mol^{-1}) [28]. In the stress ranges and temperatures used in this study, it is inferred that grain boundary slip accommodated by dislocation glide prevails for the NIMONIC 80A. Secondary phase precipitation within grains and grain boundaries alters Fe-Ni-Cr's accommodation mechanism for dislocation climb.

References

[1] K. Sawada, K. Kimura, F. Abe, Effect of nitrogen content on microstructural aspects and creep behavior in extremely low carbon 9Cr heat-resistant steel, ISIJ International 44 (2004) 1243–1249. https://doi.org/10.2355/isijinternational.44.1243

[2] H. C. Furtado, L. H. de Almeida, I. Le May, Microstructure evolution and creep properties of 2.25Cr-1Mo ferrite-pearlite and ferrite-bainite steels after exposure to elevated temperatures, Mat. Res. 2 (2017) 418–422. https://doi.org/10.1590/1980-5373-MR-2016-0596

[3] P. J. Ennis, W. J. Quadakkers, 9–12 % Chromium Steels: Application Limit and Potential for Further Development. In: Parsons (Ed.). Advanced Materials for 21st Century Turbines and Power Plants; The Institute of Materials: London, UK (2000), pp. 265–275.

[4] J. Berneti, B. Brada, G. Kosec, E. Bricelj, B. Kosec, F. Vodopivec, L. Kosec, Centreline formation of Nb(C,N) eutectic in structural steel, Metall. 49 (2010) 29–32.

[5] R. Kelkar, A. Andreaco, E. Ott, J. Groh, Alloy 718: Laser Powder Bed Additive Manufacturing for Turbine Applications, In: Ott E. et al. (Eds.), Proceedings of the 9th International Symposium on Superalloy 718 & Derivatives: Energy, Aerospace,

and Industrial Applications. The Minerals, Metals & Materials Series. Springer, Cham. (2018). https://doi.org/10.1007/978-3-319-89480-5_3
[6] R. Schafrik, R. Sprague, Superalloy technology – A perspective on critical innovations for turbine engines, Key Engineering Materials 380 (2008) 113–134. https://doi.org/10.4028/www.scientific.net/KEM.380.113
[7] M. Hohmann, G. Brooks, C. Spiegelhaue, Production methods and applications for high-quality metal powders and spray formed products, Acta Metall. Sin. (Eng. Lett.). 18 (2005) 15–23.
[8] Zhen-Xue Shi, Shi-Zhong Liu, Xiao-Guang Wang, Jia-Rong Li, Effects of Cr content on microstructure and mechanical properties of single crystal superalloy, Transactions of Nonferrous Metals Society of China 25 (2015) 776–782. https://doi.org/10.1016/S1003-6326(15)63663-9
[9] A. Nowotnik, Nickel-Based Superalloys, Reference Module in Materials Science and Materials Engineering. ASM International (2016).
[10] G. D. Smith, S. J. Patel, The role of niobium in wrought precipitation-hardened nickel-base alloys, Superalloys 718 (2005) 625–706. https://doi.org/10.7449/2005/superalloys_2005_135_154
[11] Xiaoming Dong, Xiaoli Zhang, Kui Du, Yizhou Zhou, Tao Jin, Hengqiang Ye, Microstructure of carbides at grain boundaries in nickel-based superalloys, Journal of Materials Science & Technology 28 (2012) 1031–1038. https://doi.org/10.1016/S1005-0302(12)60169-8
[12] M. Y. Li, S. M. Kuo, Y. T. Pan, Creep strengthening of iron-nickel-base superalloy for high-stress condition by cubo-octahedral nanoparticles precipitation. MRS Online Proceedings Library 1715 (2014) 7–12. https://doi.org/10.1557/opl.2014.680
[13] Y. Hasebe, K. Takasawa, T. Ohkawa, E. Maeda, T. Hatano, Grain Boundary Precipitation Strengthening of Phosphorus-Added Nickel-Iron Base Superalloy, Superalloys: Proceedings of the 13th International Symposium of Superalloys (2016). https://doi.org/10.1002/9781119075646.ch7
[14] Blaine Geddes, Hugo Leon, Xiao Huang, Superalloys: Alloying and Performance, ISBN 978-1-62708-414-3 (2010). https://doi.org/1031399/asm.b.sap.9781627083133
[15] Ch. Daniel, Introduction to Superalloys and their Applications – Superalloys Lecture 10. University of Manchester (2021). https://doi.org/10.48420/14541681.v1 .
[16] T. Sourmail, Precipitation in creep-resistant austenitic stainless steels, Materials Science and Technology 17 (2001) 1–14. https://doi.org/10.1179/026708301101508972
[17] N. S. Stoloff, Wrought and Powder Metallurgy (P/M) superalloys. In: ASM Handbook (Ed.), Volume 1, Properties and Selection: Irons, Steels, and High-Performance Alloys. Materials Park, OH: ASM International, (2005), pp. 1478–1527. https://doi.org/10.31399/asm.hb.v01.a0001049
[18] K. J. Ducki, Analysis of the precipitation and growth processes in a high-temperature Fe-Ni alloy, Journal of Achievements in Materials and Manufacturing Engineering 31 (2008) 226–232. BWAW-0002-0009.
[19] K. J. Ducki, Microstructural aspects of deformation, precipitation and strengthening processes in austenitic Fe-Ni superalloy (in Polish). Gliwice, Poland: Silesian University of Technology (2010).
[20] K. J. Ducki, Fatigue behaviour and creep resistance of Fe-Ni superalloy. Saarbrücken, Germany: LAP Lambert Academic Publishing. (2014). ISBN-10: 9783659195495.
[21] D. A. Balantic, M. Jenko, F. Vodopivec, R. Celin, Effect of change of carbide particles spacing and distribution on creep rate of martensite creep resistant steels, Materials and Technology 45 (2011) 555–560.
[22] X. Wu, S. Williams, D. Gong, A true-stress creep model based on deformation mechanisms for polycrystalline materials, J. Mater. Eng. Perform. 21 (2012) 2255–2262. https://doi.org/10.1007/s11665-012-0191-6
[23] A. B. Farina, R. C. N. Liberto, C. A. Barbosa: Development of New Intermediate Nickel Alloys for Application in Automotive Valves of High Performance Engines, Technical Paper 2013-01-1153. https://doi.org/10.4271/2013-01-1153
[24] T. Sugui, W. Minggang, Y. Huichen, Y. Xingfu, L. Tang, O. Benjiang, Influence of element Re on lattice misfits and stress rupture properties of single crystal nickel-based superalloys, Materials Science and Engineering A 527 (2010) 4458–4465. https://doi.org/10.1016/j.msea.2010.03.107
[25] T. Sugui, X. Jun, Z. Xiaoming, O. Benjiang, L. Jianwei, Y. Lili, W. Wuxiang, Microstructure and creep behavior of FGH95 nickel-base superalloy, Materials Science and Engineering A 528 (2011) 2076–2084. https://doi.org/10.1016/j.msea.2010.11.038
[26] Y. Xu, O. Jin, X. Xiao, X. Cao, G. Jia, Y. Zhu, H. Yin, Strengthening mechanisms of carbon in modified nickel-based superalloy Nimonic 80A, Materials Science and Engineering A 528 (2011) 4600–4607. https://doi.org/10.1016/j.msea.2011.02.072
[27] L. Z. He, Q. Zheng, X. F. Sun, H. R.Guan, Z. Q. Hu, A. K. Tieu, C. Lu, H. T. Zhu, Effect of carbides on the creep properties of a Ni-base superalloy M963, Materials Science and Engineering 397 (2005) 297–304. https://doi.org/10.1016/j.msea.2005.02.038
[28] A. R. Wazzan, Lattice and grain boundary self-diffusion in nickel, J. Appl. Phys. 36 (1965) 3596–3599. https://doi.org/10.1063/1.1703047